PNAS RESEARCH ARTICLE | ENGINEERING

Amphibious passive adaptation in untethered soft robots

Shukun Yin[a,1], Dickson R. Yao[a,1], Inho Kim[a], Wenjie Zhou[a], Wenzheng Heng[a], Wenjian Li[a], Songsong Tang[a], Xiaotian Ma[a], Yadong Xu[a], Gwangmook Kim[a], Hong Han[a], Kexin Fan[a], Chiara Daraio[a], and Wei Gao[a,2]

Affiliations are included on p. 9.

Edited by Yu Sun, University of Toronto, Toronto, Canada; received November 14, 2025; accepted March 26, 2026 by Editorial Board Member Yonggang Huang

Mobile robots are increasingly deployed in diverse settings, ranging from logistic and household applications to ecological monitoring and operation in extreme environments. In these contexts, robots must traverse diverse terrains, yet most existing designs rely on fixed morphologies that limit efficiency across domains. Biomimetic solutions emulate natural forms but cannot fully exploit engineered mechanisms, while active adaptive architectures typically require complex electronics and incur substantial energy costs. Inspired by amphibians and reptiles, we developed AdaptBot, an untethered adaptive soft robot that integrates rigid machinery with responsive soft materials to achieve passive reconfiguration for amphibious locomotion. AdaptBot employs a single bioinspired photothermal artificial muscle (PAM) to power multiple gaits by light, a fast and large swelling hydrogel (FLASH) to drive passive fin deployment in water, and a ratcheting transmission to convert reciprocating PAM motion into forward locomotion. These elements enable multimodal performance—including rolling, load-carrying, climbing, and paddling—under wireless control across terrestrial, aquatic, and transitional environments. Remarkably, following fin deployment, AdaptBot's swimming speed increased by 780%, demonstrating that passive adaptation is an effective strategy to enhance locomotor efficiency in robots operating in unstructured and dynamic environments.

passive adaptation | soft robotics | amphibious locomotion | artificial muscle | swelling hydrogel

Significance

Adaptive robots are needed for operation across land and water boundaries, yet most systems require complex electronics or multiple actuators. Here, we present AdaptBot, that demonstrates passive, environment-driven reconfiguration using a single light-powered artificial muscle, a fast large-swelling hydrogel that deploys fins in water, and a ratcheting transmission that converts reciprocation into forward motion. The robot rolls, climbs, tows loads, and paddles under wireless control across terrestrial, aquatic, and transitional settings, and its swimming speed increases by 780% after fin deployment. This materials and mechanisms framework reduces control complexity and power demands, enabling scalable, untethered platforms for ecological monitoring, disaster response, and other missions in unstructured environments.

Organisms that occupy a particular habitat commonly evolve highly specialized anatomical structures and morphologies that maximize locomotor efficiency—an adaptive outcome of evolution by natural selection (1). Plants, for example, exhibit tropisms that align growth with environmental cues (2). The principle of environmental specialization extends to mobile robots, which are usually confined to either terrestrial or aquatic domains (3). Similar to amphibians and certain semiaquatic reptiles that operate effectively in both media, amphibious robots capable of seamless locomotion on land and in water could markedly expand their operational envelope (4–7). Such robots are poised to enable transformative applications in radically changing environments, including ecological monitoring, disaster response, and exploration of unstructured or extreme environments (8–16).

Conventional robotic architectures typically feature fixed, invariant structures (5, 17–19). Achieving real-time reconfiguration demands compressing the slow evolutionary process into engineered mechanisms capable of continuous shape-morphing, with demonstrable improvements in performance metrics such as speed or efficiency (3). Biomimetic strategies provide one route, as seen in amphibians like frogs and salamanders: Interdigital webbing folds to reduce drag on land but expands in water to create large paddling surfaces (20). Yet biomimicry alone cannot capitalize on the capabilities of engineered materials and mechanisms, which often surpass biological performance (21). Gears, for instance, enable efficient, reversible torque transmission. Automobile wheels approach pure rolling with negligible frictional losses and avoid the repeated accelerate–decelerate "lift-and-place" cycle of animal gaits, yielding steady energy use. Paddle wheels on side-wheel steamers have simple mechanics that deliver continuous thrust in water without complex coordination. These examples highlight the rich opportunities that arise when biological inspiration is combined with mechanical efficiency.

To date, most adaptive robots rely on active mechanisms, in which shape changes are initiated by control inputs from onboard hardware (*SI Appendix*, Table S1) (21–30). In contrast, passive adaptive robots, which directly harness environmental stimuli to induce functional morphological change, remain comparatively rare. They derive both the driving force and the energy for deformation directly from environmental stimuli—such as mechanical vibrations, heat, light, humidity, and chemical gradients—thereby minimizing dependence on bulky electronics, embedded sensors, and external power supplies (31–35). The central challenge is to mechanically program these mechanisms to achieve large,

Author contributions: S.Y., D.R.Y., C.D., and W.G. designed research; S.Y., D.R.Y., I.K., W.Z., W.H., W.L., S.T., X.M., Y.X., G.K., H.H., and K.F. performed research; S.Y., D.R.Y., I.K., and W.G. analyzed data; and S.Y. and W.G. wrote the paper.

The authors declare no competing interest.

This article is a PNAS Direct Submission Y.S. is a Guest Editor invited by the Editorial Board.

[1]S.Y. and D.R.Y. contributed equally to this work.

[2]To whom correspondence may be addressed. Email: weigao@caltech.edu.

This article contains supporting information online at https://www.pnas.org/lookup/suppl/doi:10.1073/pnas.2532988123/-/DCSupplemental.

Published April 21, 2026.

reversible deformations while preserving operational robustness across environments (3, 36, 37). Stimuli-responsive hyperelastic materials, notably hydrogels and liquid crystal elastomers (LCEs), are particularly promising for this purpose (38–42). Beyond prescribing shape deformation, enhancing their speed, amplitude, and durability is key to realizing practical adaptability.

Here, we present AdaptBot, a fully integrated soft robot that combines biomimetic design with rigid mechanical components and intelligent soft materials. AdaptBot incorporates a 3D-printed chassis, wheel hubs, fins, photothermal artificial muscles (PAMs), and a laser-cut, fast and large swelling hydrogel (FLASH). While the PAMs enable untethered actuation using near-infrared (NIR) light, the FLASH provides rapid, high-amplitude, water-triggered deformation for passive adaptation (Fig. 1 *A* and *B* and *SI Appendix*, Figs. S1–S3). AdaptBot is designed around a general amphibious locomotion principle in which aquatic propulsion benefits from increased wetted surface area, whereas terrestrial locomotion favors compact geometries that minimize interference with rolling. This principle is implemented by passively deployable fins that extend in water and retract upon returning to land, enabling multimodal locomotion, including rolling, load-carrying, climbing, and paddling, across land, water, and transition zones.

AdaptBot's wheel hub unifies principles from automotive wheels and paddle wheels: On land, the outer rim rolls with minimal slip; in water, hub-mounted blades generate thrust. Three deployable fins, connected via FLASH inserts, passively extend in water and retract upon returning to land, modulating propulsive surface area to improve aquatic performance while preserving efficient terrestrial rolling (Fig. 1 *C* and *D*). Motivated by the structure and function of human musculature, the PAMs consist of 3D-printed LCE/carbon nanotube (CNT) composite fiber bundles that contract under photothermal input of an NIR lamp or laser, enabling untethered operation without onboard energy storage (Fig. 1 *C* and *E*). As an illustrative biological example of area modulation across media, anurans deploy interdigital webbing to increase effective paddle area in water and reduce it on land; Analogously, AdaptBot's fins enlarge the propulsive surface in water through passive deployment (Fig. 1 *C* and *F*). Finally, a ratcheting transmission, based on

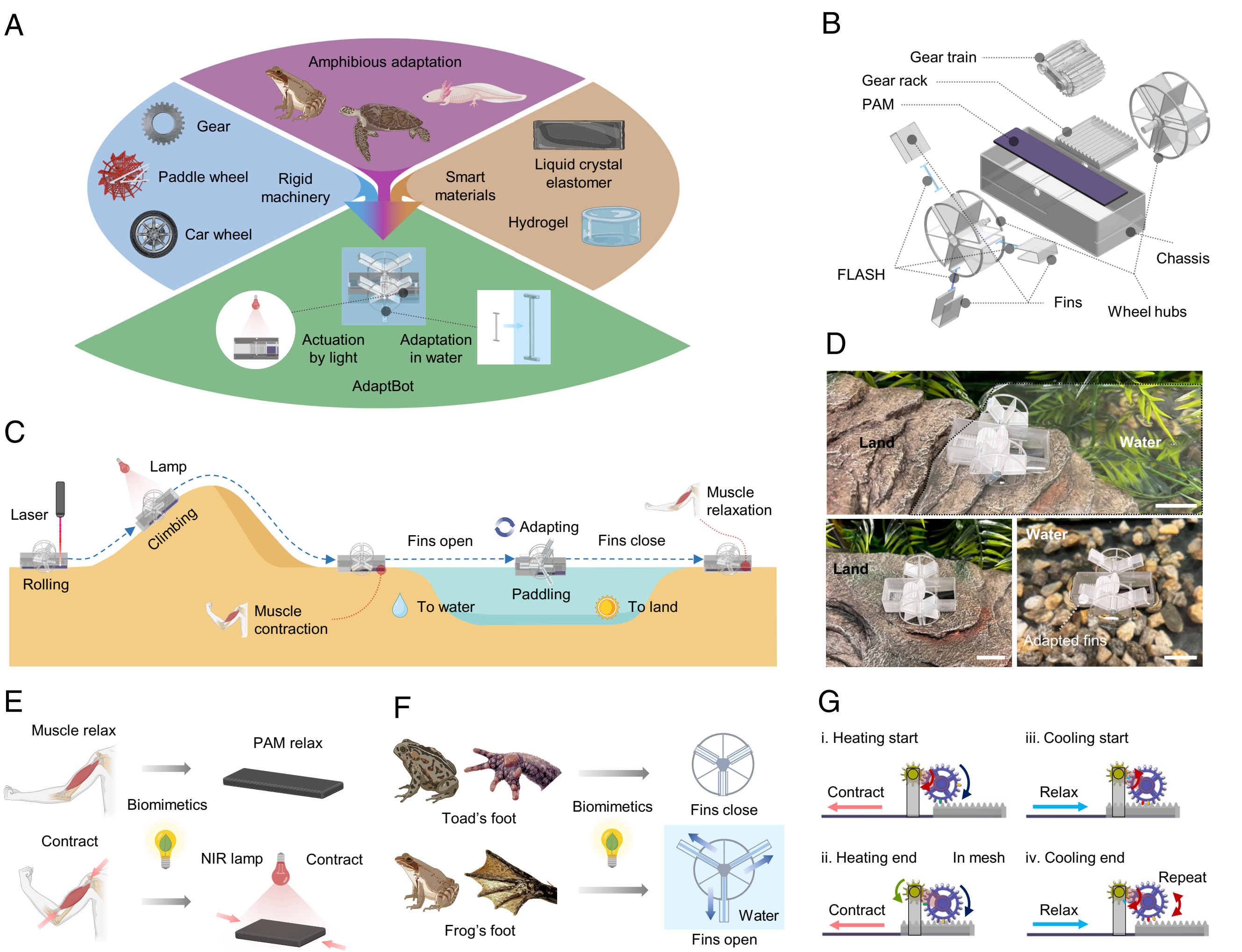

Fig. 1. AdaptBot, a passively adaptive soft robot for amphibious locomotion. (*A*) Biological and engineering inspirations for AdaptBot. Amphibious animals modulate effective propulsive area across media, increasing wetted area for aquatic propulsion while adopting compact geometries on land. In engineered systems, wheels provide efficient terrestrial rolling, while paddle wheels deliver aquatic propulsion. Smart materials such as liquid crystal elastomers (LCEs) and hydrogels respond to environmental stimuli (e.g., light, humidity), enabling AdaptBot to actuate with light and adapt in water. (*B*) Exploded schematic of AdaptBot showing chassis, wheel hubs, fins, FLASH inserts, gear train, and PAM actuator. (C) Schematic of amphibious locomotion and adaptation: AdaptBot rolls on land, passively deploys fins upon entering water to paddle, and retracts upon returning to land. (*D*) Images of AdaptBot transitioning across environments: at the land–water interface (*Top*), on land (*Bottom Left*), and in water (*Bottom Right*). (Scale bars, 2 cm.) (*E*) PAM, bioinspired by human muscle, contracts under near-infrared (NIR) light and relaxes upon cooling. (*F*) Adaptive fins, illustrated by anuran interdigital webbing that increases effective paddle area in water and reduces it on land. In AdaptBot, fins close on land and open in water. (*G*) Ratcheting transmission system converts PAM contraction–relaxation cycles into unidirectional wheel rotation.

an epicyclic gear train and gear rack, converts the contraction–relaxation cycles of a single PAM into continuous multimodal locomotion without complex control systems (Fig. 1*G*). Unlike active morphing robots that rely on sensing and feedback control, AdaptBot demonstrates that environmental stimuli alone can trigger functional reconfiguration that directly enhances locomotor performance across environments.

Results

Fabrication and Characterization of PAMs. LCEs are soft, anisotropic materials capable of large, reversible shape changes under various stimuli (43–47). In AdaptBot, the PAM, with LCE as its primary component, serves as the core actuator to drive locomotion. The PAM is anchored between the chassis and a gear rack; under intermittent NIR illumination, it drives reciprocating rack motion (Fig. 2*A* and *SI Appendix*, Fig. S2).

We fabricated PAMs using direct ink writing (DIW) to realize spatially programmed nematic order (Fig. 2 *B* and *C* and *SI Appendix*, Fig. S4 and S5, and Movie S1). To maximize actuation strain and photothermal conversion efficiency, we formulated a photopolymerizable, solvent-free LCE/CNT ink via aza-Michael addition of reactive mesogens with amine linkers (42). During DIW, the ink is heated to an isotropic, orientationally disordered state with suitable viscosity and viscoelasticity for printing fidelity and extruded through a 250 μm diameter nozzle (48). The shear and extensional flows align the mesogenic domains along the print path. Reactive acrylate end groups enable ultraviolet (UV)-induced crosslinking, locking in the prescribed director alignment (42). In the nematic temperature range (including ambient), this alignment constrains the polymer backbone into an extended conformation. Upon photothermal heating above the nematic-to-isotropic transition temperature (T_{ni}), alignment is lost and the backbone relaxes to a random-coil conformation, producing macroscopic contraction parallel to the director and expansion transverse to it (49, 50).

Printing resolution depends on both ink temperature and nozzle translation speed, quantified by the printed line width. Excessive heating softens the syringe, while insufficient heating raises viscosity—both leading to unstable printing evidenced by larger relative line-width errors (*SI Appendix*, Fig. S6). Similarly, overly slow speeds cause ink accumulation, whereas overly fast speeds create discontinuities. Optimal parameters were 20 mm s^{-1} and 70 °C, yielding lines with a mean width of 107.0 μm and low variability (Fig. 2*D* and Movie S2).

LCEs alone exhibit relatively high NIR reflectance, whereas CNTs strongly absorb in the NIR range (51–55). Homogeneous CNT dispersion within the LCE reduced reflectance (Fig. 2*E*). At 0.3 wt.% CNT, PAMs balanced strong NIR absorption with reliable printability, avoiding nozzle clogging at higher loadings (*SI Appendix*, Figs. S7 and S8). Under NIR irradiation, these PAMs generated an actuation stress of 0.16 MPa, substantially higher than CNT-free or low-loading controls (Fig. 2*F*). They reached a maximum strain of 44% at 121 °C, with no further increase upon continued heating (Fig. 2*G*). A PAM with an 8 mm^2 cross-section successfully lifted a 50 g weight with ~42% strain, while surface temperatures exceeded 125 °C (Fig. 2*H* and Movie S3). The PAMs maintained a stable actuation-stress output over 100 cycles under a fixed protocol of 20 s NIR lamp on followed by 40 s lamp off per cycle, without observable performance degradation (Fig. 2*I*).

Together, these results confirm that AdapBot's PAMs exhibit strong photothermal responsiveness, large actuation strain, and robust cycling durability, sufficient for reliable actuation in multimodal locomotion.

Design and Characterization of Ratcheting Transmission. To convert the reciprocating motion of the PAM into continuous forward translation, we designed a ratcheting transmission composed of an epicyclic gear train and a rack. In this system, the small gear is fixed in position and rigidly coupled to the wheel so that rotation about the axle drives the wheel; it functions as the sun gear. The large gear, which engages both the sun gear and the rack, is linked to the sun via two carriers. This configuration allows the large gear to spin about its axis while revolving around the sun gear with the carriers—therefore serving as the planet gear (*SI Appendix*, Fig. S9).

A representative heating–cooling cycle illustrates the mechanism's operation. As heating begins, the PAM contracts and pulls the rack leftward (Fig. 2*J*, first row; Fig. 2*K*, 0 to 27 s; Movie S4). The rack force induces clockwise rotation of the planet gear, which in return applies torque on the carriers, causing the carrier–planet assembly to rotate clockwise. Once the planet is tightly engaged with the rack, the carrier and planet maintain their positions while torque is transmitted to the sun gear, driving the wheel forward until heating ends—marked by the tooth engagement shifting from "green" to "yellow" (Fig. 2*J*, second row; Fig. 2*K*, 27 to 71 s; Movie S4). During cooling, the PAM relaxes and drives the rack rightward, imposing a counterclockwise torque on the planet and consequently a counterclockwise rotation of the carrier–planet assembly. This motion initiates disengagement between the rack and planet gear (Fig. 2*J*, third row; Fig. 2*K*, 71 to 94 s; Movie S4). Experimentally, the planet gear rotates counterclockwise from the "yellow" to the "red" tooth, then ceases self-rotation as rack–planet contact weakens. Relative sliding between the rack and planet gear alters the torque direction, producing a small clockwise oscillation of the carrier–planet assembly. This allows the "red" tooth to drop into the next rack space, resetting the system (Fig. 2*J*, fourth row; Fig. 2*K*, 94 to 100 s; Movie S4). Thus, during the rightward stroke, the carrier–planet assembly executes a sequence of small oscillatory rotations about the sun gear until the PAM returns to its original length. Performance characterization revealed a direct correspondence between PAM strain and wheel rotation angle (Fig. 2*L*), as well as the clear relationship between the input force from the PAM and output traction at the wheel rim (which propels AdaptBot forward) (Fig. 2*M*).

Synthesis and Characterization of FLASH. To accommodate environment-driven shape change, particularly in liquid environments, we sought a material capable of rapid, large-amplitude deformation in water quickly and conspicuously. At the same time, the material must maintain robust mechanical properties such as high modulus, toughness, and fatigue resistance to withstand repeated adaptations without damage. Hydrogels are attractive candidates because osmotic swelling in water can provide the actuation force. However, conventional hydrogels typically suffer from low actuation stress, slow response, and a low fatigue threshold (56). Superporous hydrogels can swell rapidly and extensively but are usually very brittle and mechanically weak (57, 58). Other strategies, such as membrane encapsulation or integration with electrodes, can enhance actuation stress but complicate fabrication and miniaturization (56, 59).

To overcome these limitations, we designed FLASH, a hydrogel that achieves rapid and substantial water-triggered swelling while maintaining mechanical robustness (Fig. 3*A*). FLASH is primarily composed of poly(acrylamide-co-sodium acrylate), P(AAm-co-NaAc), and poly(ethylene glycol) (PEG). In addition to its polymer chemistry, FLASH exhibits a porous double-network microstructure that provides interconnected transport pathways, facilitating rapid water exchange and contributing to fast swelling and deswelling kinetics

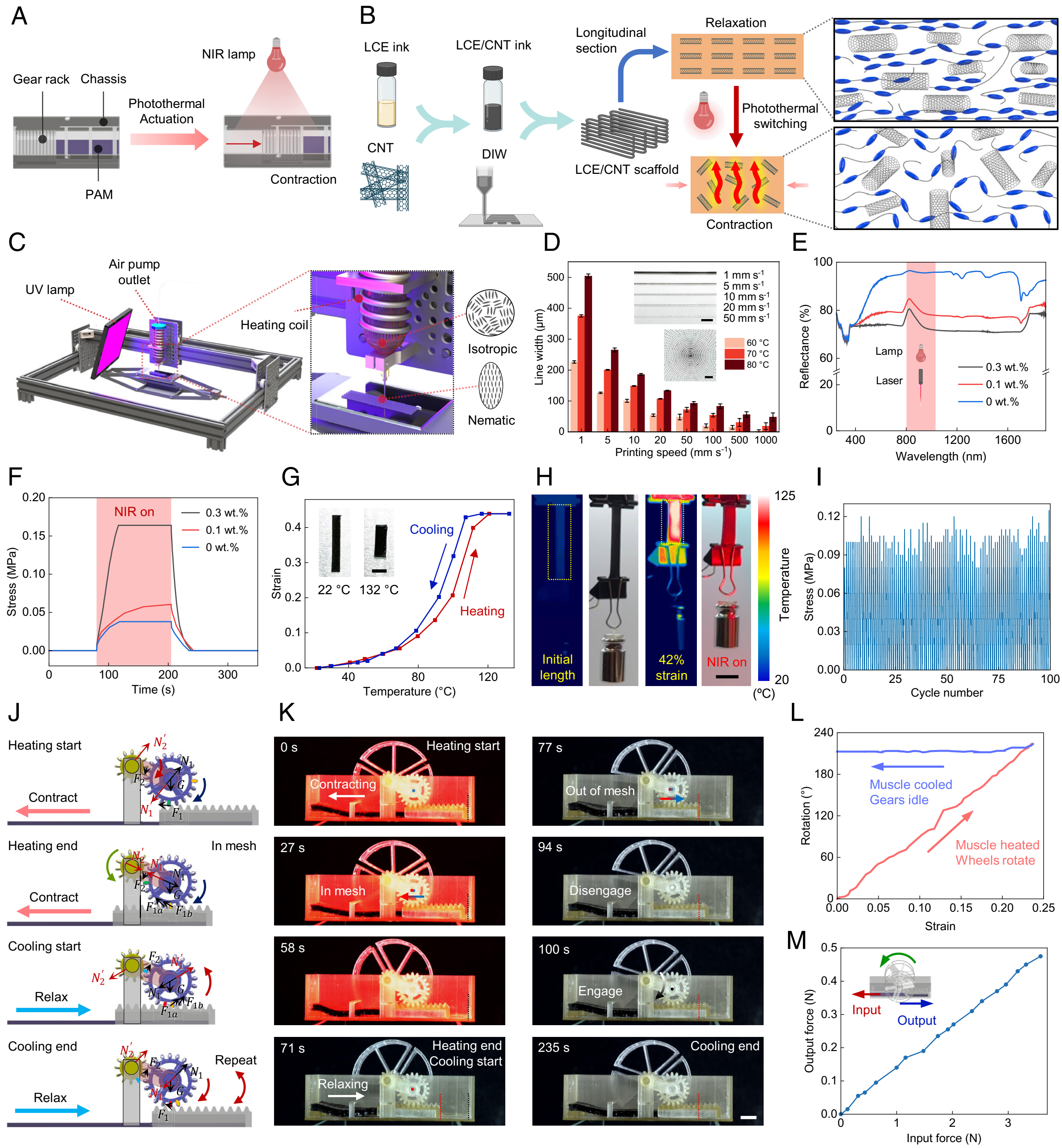

Fig. 2. Characterization of AdaptBot's PAM and ratcheting transmission. (*A*) Schematic of PAM-based photothermal actuation: NIR irradiation induces contraction, while relaxation occurs upon cooling. (*B*) Synthesis and fabrication of PAM. LCE/CNT ink is formulated, patterned by DIW, UV crosslinked, and aligned to form anisotropic scaffolds that contract under photothermal heating. CNT, carbon nanotube; DIW, direct ink writing; UV, ultraviolet. (*C*) Printing setup (*Left*) and phase transition of LCE/CNT ink during 3D printing (*Right*), showing isotropic to nematic ordering. (*D*) Printing resolution (line width) as a function of temperature and nozzle speed using a 250 μm nozzle. Insets: printed lines (*Top*) and spiral (*Bottom*) at 70°C. (Scale bar, 3 mm.) (*E*) Spectral reflectance of 0.5 mm-thick PAMs with varying CNT concentrations. The red band represents the wavelength range of the NIR lamp/laser. (*F*) Contraction stresses for PAMs with different CNT loadings under NIR irradiation (λ = 850 nm) at zero strain. (*G*) Reversible thermal actuation of a 0.3 wt.% CNT PAM during stepwise heating–cooling cycles. Insets: PAM in relaxed and actuated states. (Scale bar, 5 mm.) (*H*) Infrared and optical images of a PAM (0.8 mm thick, 1 cm wide) lifting a 50 g weight under NIR irradiation. (Scale bar, 2 cm.) (*I*) Stress output stability of PAM over 100 actuation cycles. (*J*) Schematic of ratcheting transmission mechanism converting reciprocating PAM motion into unidirectional wheel rotation. (*K*) Time-lapse snapshots of ratcheting transmission during heating–cooling cycles. (Scale bar, 0.5 cm.) (*L*) Relationship between wheel rotation angle and PAM strain during one cycle. (*M*) Relationship between PAM input force and wheel rim output force, confirming efficient force transmission.

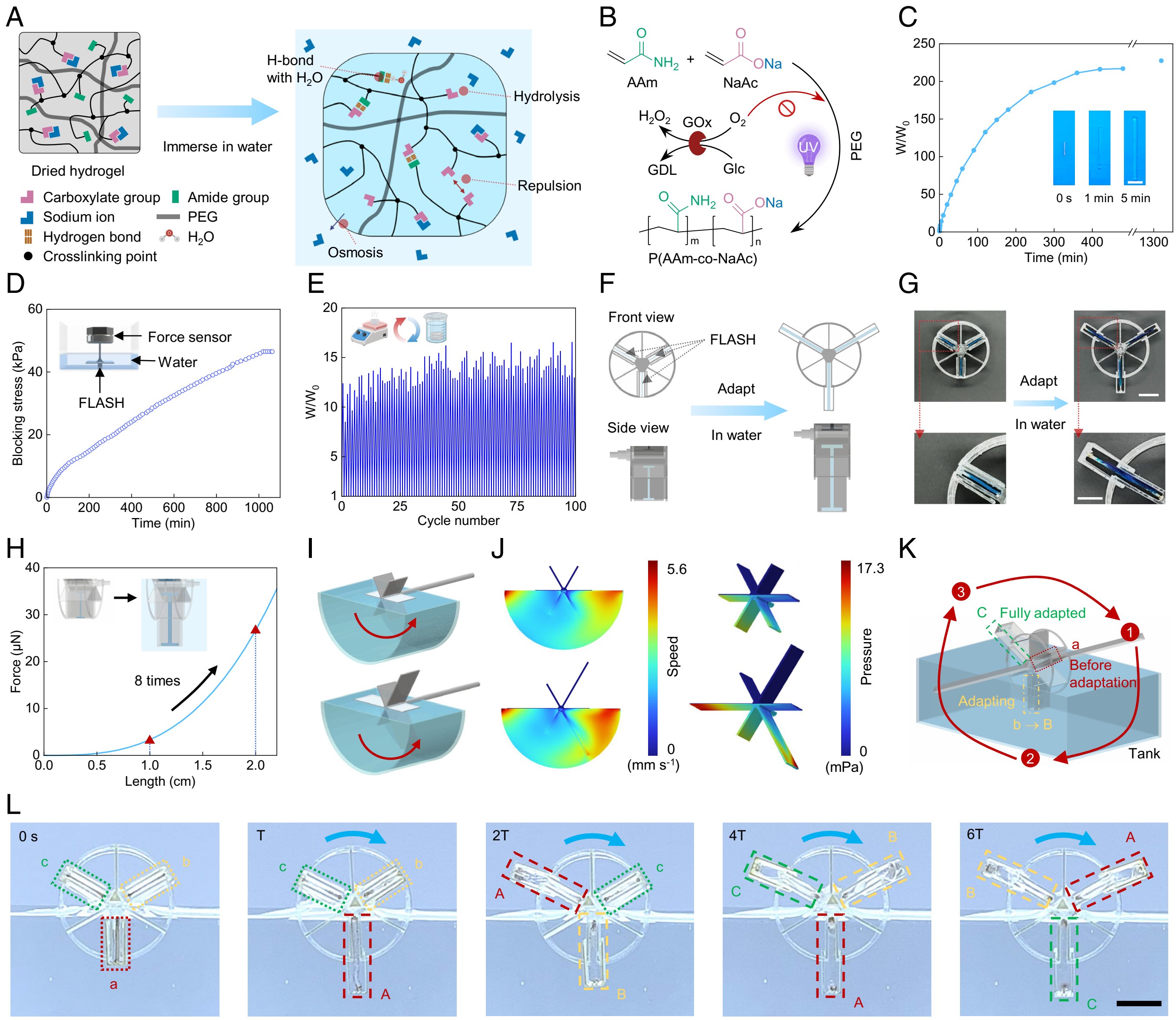

Fig. 3. Characterization of AdaptBot's FLASH inserts, adaptive fins, and wheels. (*A*) Schematic of the swelling mechanism of FLASH. (*B*) Synthesis process of FLASH by free-radical copolymerization of AAm and NaAc with PEG incorporation. AAm, acrylamide; NaAc, sodium acrylate; PEG, polyethylene glycol. (*C*) Weight changes of FLASH as a function of swelling time in water. Insets: time-lapse images of swelling. (Scale bar, 1 cm.) (*D*) Blocking stresses of FLASH during constrained swelling. Inset: schematic of force measurement setup. (*E*) Reversible swelling and drying of FLASH after initial conditioning cycles, measured over 100 actuation cycles (2 min hydration + 5 min drying on a 90 °C). Inset, schematic of the swelling and drying process. (*F*) Schematic of wheel with fins before and after FLASH-driven adaptation. (*G*) Optical images of fins and wheels before and after adaptation. [Scale bars, 1 cm (*Top*), 0.5 cm (*Bottom*).] (*H*) Theoretical calculation of propelling force on a fin as a function of its length. Inset: fin geometry before and after extension. (*I*) Schematic of the simulation setup, before (*Top*) and after (*Bottom*) adaptation. (*J*) Numerical simulation results of speed distribution of water in half cylinder (*Left*) and pressure distribution of fins (*Right*), before (*Top*) and after (*Bottom*) adaptation. (*K*) Experimental setup for fin adaptation testing in a rectangular tank. (*L*) Time-lapse sequence of fin deployment during rotation in water (T = 120 s). Lowercase letters denote unadapted fins; uppercase letters denote adapted fins. Scale bar, 1 cm.

(57, 58, 60). Its fast and large swelling originates from three factors: i) hydrolysis generates a high concentration of sodium ions along polyacrylate chains, creating strong osmotic pressure that drives water influx (61); ii) electrostatic repulsion between negatively charged carboxylate groups expands the polymer network, promoting pronounced volumetric swelling; and iii) hydrophilic amide groups on polyacrylamide form hydrogen bonds with water and, upon partial hydrolysis, generate additional carboxylate groups that further enhance water uptake (61).

FLASH also exhibits exceptional mechanical performance. In general, dense covalent crosslinking increases modulus but compromises the fatigue tolerance (62). Instead, FLASH employs long-chain covalent backbones crosslinked with domains of reversible physical interactions (hydrogen bonds and hydrophobic associations) to simultaneously achieve high modulus, toughness, and fatigue resistance (62). The three long-chain components—PAAm, PNaAc, and PEG—provide stiffness and elasticity, while their entangled networks form abundant reversible hydrogen bonds. These involve amide groups on PAAm (–$CONH_2$), ether linkages in PEG (–CH_2OCH_2–), and a fraction of nonionized carboxyl groups (–COOH) on PNaAc. Because hydrogen bonds are weaker than covalent bonds, they rupture first under stress, enabling chain stretching, disentanglement, and sliding that dissipate energy, mitigate stress concentration, and retard crack propagation. This artificial mechanism underlies FLASH's high toughness and elevated fatigue threshold (62).

FLASH is synthesized by free-radical copolymerization of AAm and NaAc with PEG incorporated (Fig. 3*B*). To suppress oxygen inhibition—which typically causes poorly cured surface layers—we introduced glucose and glucose oxidase to consume residual oxygen, enabling accurate replication of mold geometries and improving UV curing fidelity (63–65). After overnight curing, the hydrogels were dried at 60 °C and laser-cut into inserts for integration into wheel hubs and fins (*SI Appendix*, Fig. S10).

FLASH demonstrates rapid and robust actuation. Note that the swelling ratio is defined as W_{max}/W_0, and the swelling rate is quantified by the rate constant k in the equation $dW/dt = k(W_{max} - W)$, where W_0 is the initial weight of the FLASH, W_{max} is the fully swollen weight, and W is the weight at swelling time t. Upon immersion, its length doubles within 1 min, ultimately reaching an equilibrium swelling ratio of ~227 (Fig. 3*C* and *SI Appendix*, Fig. S11). Consistent with the porous network morphology, as revealed by freeze-dried scanning electron microscope (SEM) images, FLASH exhibits a swelling ratio that exceeds that of most bulk hydrogels and swells rapidly (*SI Appendix*, Figs. S12 and S14). Water temperature and chemistry can influence hydrogel swelling in realistic aquatic environments. To assess environmental robustness, we quantified FLASH swelling kinetics under controlled variations in temperature, salinity, and pH (*SI Appendix*, Fig. S13). In all tested conditions, FLASH exceeded the minimum swelling ratio required for fin deployment, demonstrating functional robustness across a broad range of aquatic settings. Ingestible and electroosmotic hydrogels both employ external membranes, making their fabrication more complex (56, 59). FLASH also delivers an actuation force markedly higher than that of most hydrogel actuators (*SI Appendix*, Table S2). Although a superporous hydrogel achieves excellent swelling ratio and fast swelling rate, it does not generate sufficient actuation force (57). Electroosmotic hydrogel can provide ample force, but its requirement for integrated electrodes and an external electric field makes it unsuitable for AdaptBot (56). A 1 cm^3 dry sample generates an actuation force of 4.65 N, corresponding to a maximum blocking stress of 46.5 kPa during swelling (Fig. 3*D*). After initial conditioning, FLASH was subjected to 100 swelling–drying cycles (2 min hydration + 5 min drying at 90 °C) and maintained a stable swelling ratio without measurable performance degradation (Fig. 3*E*).

Together, these results establish FLASH as a fast, high-amplitude, and mechanically durable hydrogel actuator well suited for enabling AdaptBot's passive adaptation in aquatic environments.

Wheel and Fin Design for Passive Adaptation. The adaptive wheel consists of a hub, three FLASH inserts, and three fins. The hub carries six blades, with three incorporating guide slots that allow fins to slide. Each FLASH insert is bonded at both ends to the hub and its corresponding fin. In the dry state, FLASH remains stiff, locking the fins in place. Upon immersion in water, FLASH rapidly swells, and the resulting expansion force drives the fin radially outward (Fig. 3 *F* and *G*). When fully extended, hooks at the fin tips interlock with the hub slot, preventing detachment and resisting torque and centrifugal forces during rotation (*SI Appendix*, Fig. S2).

When the blade face is perpendicular to the water surface, the hydrodynamic thrust is given by:

$$F = \frac{1}{6}\rho C_D c \omega^2 R^3$$

where ρ is the water density, C_D the blade drag coefficient, c the chord width, ω the angular velocity, and R the blade length. With blade width and angular velocity fixed, thrust scales with R^3. Thus, when the fins fully extend and effectively double the blade length, the thrust of each blade increases by a factor of eight (Fig. 3*H* and *Numerical Computation and Simulation*).

The thrust enhancement with fully deployed fins was further confirmed by simulation. As shown in Fig. 3*I*, adapted and unadapted wheels rotate counterclockwise at the same angular speed in a semicylindrical water tank. Computational fluid dynamics (CFD) analysis of the flow velocity field (Fig. 3*J*) revealed that the adapted wheel displaced a larger volume of water and generated higher flow speeds. Before adaptation, the maximum local water velocity was 4.5 mm s^{-1}; after adaptation, it increased to 5.6 mm s^{-1}. Corresponding pressure maps showed increased edge pressures on the adapted blades, confirming that water exerted greater hydrodynamic thrust after fin deployment. The maximum pressure on the blade surface rose from 8.6 mPa (unadapted) to 17.3 mPa (adapted).

The deployment process was validated experimentally. In the test setup (Fig. 3*K*), triangular struts at the wheel centers supported the wheel above the tank. During testing, the wheel was rotated by 120° every 2 min to simulate motion. As shown in Fig. 3*L* and Movie S5, after 480° of rotation (8 min), all three fins achieved full extension, and after an additional 240° (4 min), none detached or retracted. These results confirm that the fins deploy smoothly upon water exposure, and once extended, maintain a stable configuration throughout operation.

In addition, fin retraction during deswelling was characterized. A wheel with three fully deployed fins retracted completely within 23 min when placed on a 90 °C hot plate, confirming reversible fin stowage after water exposure (*SI Appendix*, Fig. S15 and Movie S6).

Demonstration of Amphibious Passive Adaptation. To rigorously evaluate AdaptBot's multimodal, amphibious locomotion and passive adaptation capability, we designed a sequence of representative scenarios.

First, terrestrial rolling was tested (Fig. 4*A* and *SI Appendix*, Fig. S16*A* and Movie S7). One locomotion cycle was defined as NIR illumination until the PAM achieved at least 50% of its maximum strain, followed by lamp-off until the PAM returned to its original length. This definition reflects the fact that, under load, attaining theoretical maximum strain is considerably more difficult than in the unloaded state, while excessively long NIR exposure could risk thermal degradation of the actuator. Under these conditions, AdaptBot exhibited a mean cycle time of 77.5 s, and after 10 cycles, it had advanced 2.5 body lengths, with an average speed of 0.16 mm s^{-1}. We further verified that rolling speed increases with delivered NIR power. By reducing lamp standoff distance, the instantaneous peak rolling speed reached 0.24 mm s^{-1} (*SI Appendix*, Fig. S17 and Movie S8).

AdaptBot's wireless, untethered actuation can be realized at standoff distances. An NIR lamp provides spatially uniform heating of the PAM; however, to ensure adequate power delivery, the lamp must be positioned within 30 cm of the actuator (*SI Appendix*, Fig. S18). In contrast, an NIR laser maintains collimation over meter-scale distances and therefore delivers substantially higher power at range; with laser illumination at distance > 1 m, AdaptBot advanced reliably (*SI Appendix*, Fig. S19 and Movie S9). Nevertheless, because the laser spot is small relative to the PAM footprint, energy deposition is highly localized, producing steep temperature gradients that can carbonize the composite and initiate fracture. In principle, this limitation can be mitigated by distributing the delivered energy in space and time. Increasing the beam footprint or shaping the beam toward a more uniform intensity profile reduces peak power density, while beam scanning (e.g., galvanometric mirrors or motion-controlled stages) time-averages heating to prevent sustained hot spots (66). However, for stability and repeatability, subsequent experiments still employed the NIR lamp.

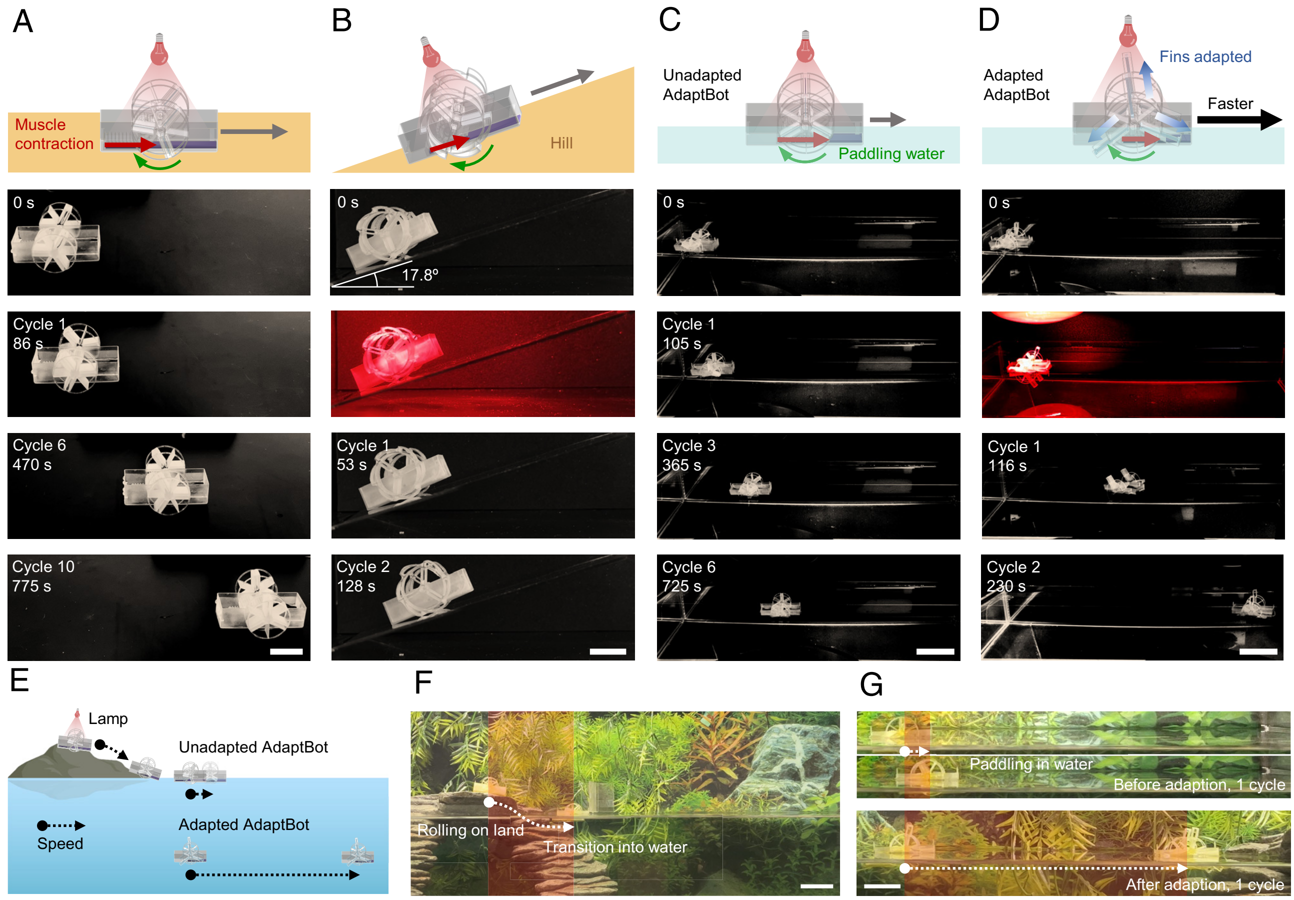

Fig. 4. Demonstration of AdaptBot's amphibious locomotion and passive adaptation across environments. (*A*) Locomotion on flat ground. *Top*: schematic of rolling driven by PAM contraction/relaxation. *Bottom*: time-lapse sequence over 10 cycles, showing forward displacement. (Scale bar, 2 cm.) (*B*) Climbing on a 17.8° incline. *Top*: schematic of hill-climbing strategy. *Bottom*: time-lapse sequence over two cycles, showing slope ascent aided by wheel design and Dragon Skin coating. (Scale bar, 2 cm.) (*C*) Swimming with fins stowed (unadapted state). *Top*: schematic of paddling with reduced surface area. *Bottom*: time-lapse sequence showing slow propulsion over six cycles. (Scale bar, 5 cm.) (*D*) Swimming with fins deployed (adapted state). *Top*: schematic of enhanced propulsion with expanded surface area. *Bottom*: time-lapse sequence over two cycles, showing markedly faster progression. (Scale bar, 5 cm.) (*E*) Schematic of the ecological tank used for hybrid locomotion tests. (*F*) Composite images of AdaptBot rolling on land and transitioning into water. (Scale bar, 5 cm.) (*G*) Composite images of AdaptBot swimming before and after fin deployment, showing increased swimming distance per cycle following passive adaptation. (Scale bar, 3 cm.)

To address both the hot-spot limitation of focused laser irradiation and the standoff constraint of lamp illumination, we implemented an electrothermal LCE actuator incorporating an embedded serpentine resistive heater (*SI Appendix*, Fig. S20). In this configuration, Joule heating is generated internally within the actuator and does not rely on optical power delivery at a distance. The electrothermally heated actuator produces uniform contraction and successfully drives AdaptBot locomotion under electrical input (*SI Appendix*, Figs. S21 and S22 and Movies S10 and S11).

The combination of PAM-based actuation and efficient transmission enables AdaptBot to handle payloads of 6.0 times its own mass. In towing tests, AdaptBot (8.76 g) moved forward under NIR lamp actuation while pulling a cart plus a weight totaling 52.23 g (*SI Appendix*, Fig. S23 and Movie S12).

We next assessed climbing performance on an incline (Fig. 4*B* and *SI Appendix*, Fig. S16*B* and Movie S13). In this case, gravity exerted a downslope force component that introduced counterclockwise torque on the wheels, which in turn prevented the ratcheting transmission from functioning properly during the cooling phase—causing AdaptBot to backslide as the PAM relaxed. To address this, we engineered wheels with low forward rolling resistance and high reverse resistance, and applied a Dragon Skin coating to increase surface friction. Additionally, to ensure adequate power delivery, the NIR lamp was positioned closer to AdaptBot during climbing than rolling on flat ground. With these modifications, AdaptBot successfully climbed a 17.8° incline, achieving a mean cycle time of 64 s and advancing 0.46 body lengths after two cycles, with an average speed of 0.18 mm s^{-1}.

To further evaluate locomotion across heterogeneous natural terrains, we equipped AdaptBot with high-traction wheels featuring a paddle-tire-style tread pattern commonly used in industrial vehicles to enhance traction on loose substrates. With these wheels, AdaptBot demonstrated rolling locomotion on sandy area, moist ground, and wetland conditions (*SI Appendix*, Fig. S24 and Movie S14). These results illustrate substrate-specific modular optimization in addition to the incline-oriented wheel modification used for slope climbing. Together with passive fin deployment in water, this modularity enables locomotion across diverse terrestrial and land–water transition environments.

We then compared aquatic locomotion with fins stowed versus fully deployed (Fig. 4 *C* and *D* and *SI Appendix*, Fig. S16 *C* and *D* and Movie S15), while keeping NIR illumination time per cycle approximately constant. In the unadapted state, with fins retracted, AdaptBot advanced only 2.3 body lengths over six cycles, with a mean cycle time of 120.8 s and an average speed of 0.16 mm s^{-1}. In contrast, once the fins were passively deployed in water, AdaptBot advanced 6.4 body lengths in two cycles, with a mean cycle time of 115.0 s and an average speed of 1.4 mm s^{-1}, which compares favorably with many reported light-driven soft robots

(*SI Appendix*, Table S3). This corresponds to an average swimming speed 7.8 times greater than that in the unadapted case, demonstrating the substantial efficiency gains enabled by fin adaptation.

In the current design, direct self-extraction from deep water onto dry ground remains challenging when the fins are fully deployed, due to increased drag and contact area. A plausible operational scenario involves gradual water-level recession (e.g., tidal or shoreline transitions), where the robot becomes exposed on saturated terrain and FLASH begins to deswell, allowing fins to retract. Consistent with this use case, AdaptBot demonstrated rolling locomotion under wetland-like conditions (*SI Appendix*, Fig. S24 and Movie S14). During NIR-lamp-driven locomotion after water exposure, fin retraction was facilitated over two heating cycles, resulting in largely stowed fins (*SI Appendix*, Fig. S25 and Movie S16).

Finally, we examined locomotion across heterogeneous terrain in an ecological tank (Fig. 4*E*). Under intermittent NIR illumination from a lamp positioned above the robot, AdaptBot rolled across a rock, transitioned into the water (Fig. 4*F* and Movie S17), then began paddling. Following passive fin deployment, the distance traveled per cycle during swimming increased substantially compared to the preadaptation state (Fig. 4*G* and Movie S17), highlighting the system's ability to autonomously optimize performance in response to environmental transitions.

Compared with previously reported representative light-driven soft robots, AdaptBot is the only system that achieves locomotion on land, in water, on inclined surfaces, and under load (*SI Appendix*, Table S3). While enabling multimodal, multienvironment, and cross-environment operation, AdaptBot attains terrestrial, aquatic, and uphill speeds comparable to single-mode terrestrial or aquatic light-driven soft robots; its payload capacity is far greater than that of many other soft robots and hard robots of similar weight, towing loads up to six times its own body weight (67).

Discussion

We report here an untethered soft robot, AdaptBot, that leverages passive adaptation to achieve multimodal, amphibious locomotion—rolling on level ground, carrying loads, climbing slopes, and paddling in water—while markedly improving locomotor efficiency through environment-driven reconfiguration. Its bioinspired design draws on general amphibious locomotion principles observed in nature, particularly environment-dependent modulation of effective propulsive area across land and water. This comparative framework motivated the incorporation of deployable fins that enlarge the propulsive surface area in water and increase thrust, allowing intelligent behaviors across environments. At the same time, AdaptBot integrates rigid mechanical elements, combining the rolling efficiency of wheels with the thrust-generating function of paddle wheels to enable high-performance locomotion across land–water boundaries.

Crucially, AdaptBot demonstrates the value of integrating stimulus-responsive soft materials with mechanical design. The LCE, doped with CNTs and printed into aligned fiber bundles, undergoes cyclic contraction–extension under intermittent NIR illumination, enabling untethered actuation without onboard power storage. The hydrogel, FLASH, leverages hydrolysis, osmotic pressure, and ionic repulsion to swell rapidly and substantially upon immersion, deploying the fins for enhanced propulsion; upon returning to land, gradual deswelling retracts the fins, restoring terrestrial rolling. Complementing these materials, a ratcheting transmission allows multimodal locomotion using only a single actuator: The system advances during PAM contraction while resisting backsliding during relaxation. Together, these mechanisms enabled AdaptBot to exhibit a dramatic increase in aquatic speed following fin deployment, underscoring the functional advantage of passive adaptation.

More broadly, AdaptBot establishes a design framework for passively adaptive mobile robots, condensing strategies that typically arise over evolutionary timescales into an engineered mechanical paradigm. Three principles underlie this approach: i) intelligent materials harvest both the driving force and the energy for deformation directly from environmental stimuli (e.g., vibration, heat, light, humidity, and chemical gradients); ii) structural design ensures that environmentally triggered deformations translate into measurable performance gains; and iii) system-level optimization integrates rigid mechanical efficiency with biomimetic adaptability. Beyond continuous shape changes, other energy-free configuration–holding strategies—such as variable-stiffness actuators, multistable structures, or plastically deformable components—could also be incorporated into future designs.

Passive adaptation offers particular advantages in resource-constrained environments or scenarios requiring autonomous transitions across environment thresholds. Rather than deploying separate robots specialized for each environment, a single platform can adaptively navigate diverse terrains, enabling, for instance, the monitoring of endangered ecosystems or robotic exploration in extraterrestrial settings. Furthermore, passive adaptation enables substantial morphological changes for effective locomotion across multiple environments while requiring only simple control of a single actuator, rather than complex, actively controlled multiactuator systems.

We anticipate that passive adaptive designs will yield robotic systems capable of optimizing multiple performance metrics across environments, in some cases rivaling or even surpassing the adaptability of natural systems. Nonetheless, challenges remain in selecting adaptive strategies, developing deformation mechanisms with sufficient durability, and integrating passive adaptation with sensing and control. We envision that closer coupling among materials science, biology, and AI will accelerate progress toward robot platforms capable of rapid and efficient evolution.

Materials and Methods

Materials. 2-Benzyl-2-(dimethylamino)-4′-morpholinobutyrophenone (Irgacure 369), butylamine, *N,N′*-methylenebis(acrylamide) (MBA), glucose oxidase (from *Aspergillus niger*), acrylic acid (AAc), and sodium hydroxide (NaOH) were purchased from Sigma-Aldrich. Dextrose (d-glucose) anhydrous and isopropyl alcohol (IPA) were purchased from Fisher Scientific. Acrylamide (AAm) and polyethylene glycol (PEG, M_W = 6,000) were purchased from Thermal Fisher Scientific. 1,4-Bis [4-(6-acryloyloxyhexyloxy)benzoyloxy]-2-methylbenzene (RM82) was purchased from Wilshire Technologies. 2-Hydroxy-2-methylpropiophenone (Irgacure 1173) was purchased from Tokyo Chemical Industry Co. Multiwalled carbon nanotubes (CNTs) were purchased from Beijing Boyu Co. UV-sensitive 3D printing resin was purchased from Anycubic. Dragon Skin (Dragon Skin FX-Pro) was purchased from Smooth-On. Cyanoacrylate adhesive was purchased from Loctite.

Fabrication of AdaptBot.

Preparation of PAM. An LCE/CNT ink was prepared as follows. 2.00 g of liquid crystal monomer RM82, 55 mg of photoinitiator Irgacure 369, and 7 mg of CNTs (0.3 wt.%) were combined in a 20 mL glass vial. 267 μL of crosslinker butylamine was added, and the vial was sealed immediately to minimize evaporation. The mixture was heated to 100 °C and vortexed until homogeneous. Oligomerization was carried out at 80 °C for 20 h with the vial wrapped in aluminum foil to exclude ambient light. The ink was then transferred into a 10 cc amber barrel (Nordson EFD) that blocks UV/visible light, fitted with a 0.25 mm inner-diameter stainless-steel nozzle (Nordson EFD), sealed with foil, and stored at room temperature.

For DIW, ink temperature was independently controlled at both the barrel and the nozzle by two heating coils instrumented with K-type thermocouples and governed by PID temperature controllers (Tempco Co.), resulting in minimal temperature fluctuations under optimized parameters (*SI Appendix*, Figs. S4 and S5 and Table S4 and Movies S1 and S2). The barrel was connected to a pressure-driven extrusion system (Ultimus V, Nordson EFD) set to 90 psi and mounted on a closed-loop three-axis motion-control gantry (Aerotech Inc.), which maintained effectively constant nozzle translation speed during printing (*SI Appendix*, Fig. S5). PAM geometries were designed in SolidWorks and converted to G-code using slic3r. Printing was performed at 20 mm s^{-1} onto a glass substrate. A 20 W, 395 nm UV lamp was positioned 10 to 20 cm from the build plane during printing. Printed parts were postcured overnight in a 120 W UV chamber to ensure complete crosslinking.

The electrothermal LCE actuator was fabricated by embedding a laser-cut copper serpentine trace as a resistive heater within the LCE matrix. A bilayer configuration was employed, in which the copper trace was sandwiched between two LCE layers to improve mechanical symmetry and thermal uniformity (*SI Appendix*, Fig. S20). Electrical input generated Joule heating within the actuator, inducing LCE contraction. The temperature distribution was characterized by infrared thermography (*SI Appendix*, Fig. S21 and Movie S10), and the actuator was integrated into AdaptBot to drive locomotion under electrical actuation (*SI Appendix*, Fig. S22 and Movie S11).

Preparation of FLASH inserts. AAm (0.50 g), PEG (1.00 g), NaOH (0.278 g), MBA (0.010 g), glucose (0.10 g), and deionized water (9 mL) were combined in a 20 mL glass vial, vortexed, and sonicated until fully dissolved. Acrylic acid (500 μL) and Irgacure 1173 (4 μL) were then added and vortexed to homogeneity. Glucose oxidase (5 mg) was introduced next; after brief vortexing and sonication to ensure uniformity, the precursor solution was promptly injected into molds.

Mold frames were fabricated by masked stereolithography (MSLA) 3D printer (Mars 3, Elegoo Inc.). Each frame was sandwiched between two glass slides to form a closed mold (*SI Appendix*, Fig. S10). Following injection, samples were cured overnight in a 120 W UV chamber to ensure complete polymerization.

After curing, the glass slides were carefully separated and the hydrogel within the frame was trimmed free with a razor blade. The gels were dried at 60 °C overnight to yield dried hydrogel sheets, which were subsequently laser-cut (Universal Laser Systems) to produce FLASH inserts; cutting patterns were designed in AutoCAD.

Assembly of AdaptBot. All components other than the PAM and FLASH inserts were designed in SolidWorks and fabricated by MSLA 3D printing (*SI Appendix*, Fig. S2). Printed parts were rinsed with IPA and postcured for 1 h in a 120 W UV chamber. The assembly workflow is shown in *SI Appendix*, Fig. S3. First, each adaptive wheel was assembled from a hub, three FLASH inserts, and three fins. In the dry state, both ends of each FLASH insert were bonded to the hub and the corresponding fin with cyanoacrylate adhesive, fixing the fin's position relative to the hub so that the fins remain stowed and the wheel rolls smoothly (*SI Appendix*, Fig. S3*A*). Next, the epicyclic gear train—comprising a large gear, a small gear, and two carriers—was assembled using shaft–bore fits to mount the gears and ensure free rotation (*SI Appendix*, Fig. S3*B*). The PAM was then installed, with one end bonded to the chassis and the other to the gear rack (*SI Appendix*, Fig. S3*C*). Finally, the axles of two wheels were inserted through the chassis holes and bonded into the cavities flanking the small gear.

Characterization Techniques. Line widths of DIW prints were measured using an optical microscope (Zeiss AXIO Scope A1). Reflectance of PAMs with different CNT loadings was obtained with a UV–Vis–NIR spectrophotometer (Cary 5000). The actuation stress under constant strain, stress–strain curves, and the hydrogel blocking stress were measured on a tensile/compression tester (Mark-10) equipped with a 25 N force gauge. Morphological changes in the PAM and FLASH, as well as AdaptBot's locomotion, were recorded with a digital camera (Sony A7 III) and analyzed in ImageJ. PAM temperature was monitored with an infrared camera (FLIR T540). Hydrogel mass was measured on an analytical balance (Mettler Toledo). Rheological properties of the LCE/CNT ink were characterized on a rheometer (Anton Paar MCR 302). For actuation, either a 250 W, 850 nm NIR lamp (RubyLux) or a 2 W, 808 nm NIR laser (Lasever Inc.) was used.

Numerical Computation and Simulation.

Theoretical calculation of thrust of a blade. The thrust generated by a blade may be approximated by summing the local drag forces exerted by each infinitesimal blade element. For a blade of constant chord length c rotating at angular velocity ω in a fluid of density ρ, the local drag force on an annular element of width dr at radius r is given by the quadratic drag law:

$$\mathrm{d}F = \frac{1}{2}\rho C_D\left(c\mathrm{d}r\right)\left(\omega r\right)^2, \quad [\mathbf{1}]$$

where C_D is the drag coefficient of the blade profile.

Integrating from the hub ($r = 0$) to the tip ($r = R$) yields the total thrust F:

$$F = \int_0^R \frac{1}{2}\rho C_D c\omega^2 r^2 \mathrm{d}r = \frac{1}{6}\rho C_D c\omega^2 R^3. \quad [\mathbf{2}]$$

If the paddle-wheel radius is increased from R to $2R$ while holding ω, c, ρ, and C_D constant, the new thrust $F' = 8F$.

Computational fluid dynamics simulations. The commercial software COMSOL Multiphysics is utilized for computational fluid dynamics (CFD) simulations to qualitatively assess the water velocity field and the pressure distribution on the blades at the same angular velocity before and after fin adaptation.

Data, Materials, and Software Availability. All Study data are included in the article and/or supporting information.

ACKNOWLEDGMENTS. This work was supported through National Research Foundation of Korea Grant RS-2024-00411904 and Heritage Medical Research Institute (W.G.). We thank Andrew Nyholm and Harry A. Atwater, Jr. for assistance with a solar simulator. Figs. 1 *A*, *C*, *E*, and *F*, 2*B*, and 3*E* and SI Appendix, Figs. S10, and S24 were created with BioRender.

Author affiliations: [a]Division of Engineering and Applied Science, California Institute of Technology, Pasadena, CA 91125

1. F. E. Fish, Advantages of aquatic animals as models for bio-inspired drones over present AUV technology. *Bioinspir. Biomim.* **15**, 025001 (2020).
2. C. Darwin, *The Power of Movement in Plants* (D. Appleton, 1900).
3. R. Baines, F. Fish, J. Bongard, R. Kramer-Bottiglio, Robots that evolve on demand. *Nat. Rev. Mater.* **9**, 822–835 (2024).
4. D. R. Yao, I. Kim, S. Yin, W. Gao, Multimodal soft robotic actuation and locomotion. *Adv. Mater.* **36**, 2308829 (2024).
5. D. A. Paley, N. M. Wereley, Eds., *Bioinspired Sensing, Actuation, and Control in Underwater Soft Robotic Systems* (Springer International Publishing, 2021).
6. G. Dudek *et al.*, AQUA: An amphibious autonomous robot. *Computer* **40**, 46–53 (2007).
7. A. J. Ijspeert, Amphibious and sprawling locomotion: From biology to robotics and back. *Annu. Rev. Control. Robot. Auton. Syst.* **3**, 173–193 (2020).
8. S. S. Sethi, R. M. Ewers, N. S. Jones, C. D. L. Orme, L. Picinali, Robust, real-time and autonomous monitoring of ecosystems with an open, low-cost, networked device. *Methods Ecol. Evol.* **9**, 2383–2387 (2018).
9. K. Prabhakaran, R. Nagarajan, F. Merlin Franco, A. Anand Kumar, Biomonitoring of Malaysian aquatic environments: A review of status and prospects. *Ecohydrol. Hydrobiol.* **17**, 134–147 (2017).
10. K. K. Dennis *et al.*, Biomonitoring in the era of the exposome. *Environ. Health Perspect.* **125**, 502–510 (2017).
11. M. Z. Naser, Extraterrestrial construction materials. *Prog. Mater. Sci.* **105**, 100577 (2019).
12. M. Weinzierl, Space, the final economic frontier. *J. Econ. Perspect.* **32**, 173–192 (2018).
13. T. Miki *et al.*, Learning robust perceptive locomotion for quadrupedal robots in the wild. *Sci. Robot.* **7**, eabk2822 (2022).
14. N. R. Sinatra *et al.*, Ultragentle manipulation of delicate structures using a soft robotic gripper. *Sci. Robot.* **4**, eaax5425 (2019).
15. R. D'Andrea, Guest editorial: A revolution in the warehouse: A retrospective on Kiva Systems and the grand challenges ahead. *IEEE Trans. Autom. Sci. Eng.* **9**, 638–639 (2012).
16. S. Yin *et al.*, Wearable and implantable soft robots. *Chem. Rev.* **124**, 11585–11636 (2024).
17. T. F. Nygaard, C. P. Martin, J. Torresen, K. Glette, D. Howard, Real-world embodied AI through a morphologically adaptive quadruped robot. *Nat. Mach. Intell.* **3**, 410–419 (2021).
18. D. Shah *et al.*, Shape changing robots: Bioinspiration, simulation, and physical realization. *Adv. Mater.* **33**, 2002882 (2021).
19. R. J. Lock, S. C. Burgess, R. Vaidyanathan, Multi-modal locomotion: From animal to application. *Bioinspir. Biomim.* **9**, 011001 (2013).
20. J. Goldberg, M. Fabrezi, Development and variation of the anuran webbed feet (Amphibia, Anura). *Zool. J. Linn. Soc.* **152**, 39–58 (2008).
21. R. Baines *et al.*, Multi-environment robotic transitions through adaptive morphogenesis. *Nature* **610**, 283–289 (2022).
22. J. Sun, J. Zhao, An adaptive walking robot with reconfigurable mechanisms using shape morphing joints. *IEEE Robot. Autom. Lett.* **4**, 724–731 (2019).
23. J. Sun, E. Lerner, B. Tighe, C. Middlemist, J. Zhao, Embedded shape morphing for morphologically adaptive robots. *Nat. Commun.* **14**, 6023 (2023).

24. T. F. Nygaard, C. P. Martin, J. Torresen, K. Glette, D. Howard, Real-world embodied AI through a morphologically adaptive quadruped robot. *Nat. Mach. Intell.* **3**, 410–419 (2021).
25. T. Kim, S. Lee, S. Chang, S. Hwang, Y.-L. Park, Environmental adaptability of legged robots with cutaneous inflation and sensation. *Adv. Intell. Syst.* **5**, 2300172 (2023).
26. D. Hwang, E. J. Barron, A. B. M. T. Haque, M. D. Bartlett, Shape morphing mechanical metamaterials through reversible plasticity. *Sci. Robot.* **7**, eabg2171 (2022).
27. Z. Zhakypov, K. Mori, K. Hosoda, J. Paik, Designing minimal and scalable insect-inspired multi-locomotion millirobots. *Nature* **571**, 381–386 (2019).
28. Q. Ze *et al.*, Spinning-enabled wireless amphibious origami millirobot. *Nat. Commun.* **13**, 3118 (2022).
29. Y. Lai *et al.*, An agile multimodal microrobot with architected passively morphing wheels. *Sci. Adv.* **10**, eadp1176 (2024).
30. S. Xu *et al.*, Transforming machines capable of continuous 3D shape morphing and locking. *Nat. Mach. Intell.* **7**, 703–715 (2025).
31. C. Xin *et al.*, Environmentally adaptive shape-morphing microrobots for localized cancer cell treatment. *ACS Nano* **15**, 18048–18059 (2021).
32. Z. Liang *et al.*, Next-generation energy harvesting and storage technologies for robots across all scales. *Adv. Intell. Syst.* **5**, 2200045 (2023).
33. A. Kotikian *et al.*, Untethered soft robotic matter with passive control of shape morphing and propulsion. *Sci. Robot.* **4**, eaax7044 (2019).
34. M. P. da Cunha, M. G. Debije, A. P. H. J. Schenning, Bioinspired light-driven soft robots based on liquid crystal polymers. *Chem. Soc. Rev.* **49**, 6568–6578 (2020).
35. P. Li, N. Su, Z. Wang, J. Qiu, A Ti3C2Tx MXene-based energy-harvesting soft actuator with self-powered humidity sensing and real-time motion tracking capability. *ACS Nano* **15**, 16811–16818 (2021).
36. L. Ai, S. Yin, W. He, P. Zhang, Y. Li, Easy-to-actuate multi-compatible truss structures with prescribed reconfiguration. *Nat. Commun.* **15**, 4886 (2024).
37. M. Bhargava *et al.*, Computational design and fabrication of modular robots with untethered control. arXiv [Preprint] (2025), http://arxiv.org/abs/2508.05410 [Accessed 28 August 2025].
38. X. Liu *et al.*, Recent advances in stimuli-responsive shape-morphing hydrogels. *Adv. Funct. Mater.* **32**, 2203323 (2022).
39. X. Le, W. Lu, J. Zhang, T. Chen, Recent progress in biomimetic anisotropic hydrogel actuators. *Adv. Sci.* **6**, 1801584 (2019).
40. Y. Guo, J. Zhang, W. Hu, M. T. A. Khan, M. Sitti, Shape-programmable liquid crystal elastomer structures with arbitrary three-dimensional director fields and geometries. *Nat. Commun.* **12**, 5936 (2021).
41. M. Zadan *et al.*, Liquid crystal elastomer with integrated soft thermoelectrics for shape memory actuation and energy harvesting. *Adv. Mater.* **34**, 2200857 (2022).
42. A. Kotikian, R. L. Truby, J. W. Boley, T. J. White, J. A. Lewis, 3D printing of liquid crystal elastomeric actuators with spatially programed nematic order. *Adv. Mater.* **30**, 1706164 (2018).
43. T. Guin *et al.*, Layered liquid crystal elastomer actuators. *Nat. Commun.* **9**, 2531 (2018).
44. T. H. Ware, M. E. McConney, J. J. Wie, V. P. Tondiglia, T. J. White, Voxelated liquid crystal elastomers. *Science* **347**, 982–984 (2015).
45. I. H. Kim *et al.*, Human-muscle-inspired single fibre actuator with reversible percolation. *Nat. Nanotechnol.* **17**, 1198–1205 (2022).
46. A. Kotikian *et al.*, Untethered soft robotic matter with passive control of shape morphing and propulsion. *Sci. Robot.* **4**, eaax7044 (2019).
47. E. C. Davidson, A. Kotikian, S. Li, J. Aizenberg, J. A. Lewis, 3D printable and reconfigurable liquid crystal elastomers with light-induced shape memory via dynamic bond exchange. *Adv. Mater.* **32**, 1905682 (2020).
48. A. Kotikian *et al.*, Innervated, self-sensing liquid crystal elastomer actuators with closed loop control. *Adv. Mater.* **33**, 2101814 (2021).
49. T. J. White, D. J. Broer, Programmable and adaptive mechanics with liquid crystal polymer networks and elastomers. *Nat. Mater.* **14**, 1087–1098 (2015).
50. K. M. Herbert *et al.*, Synthesis and alignment of liquid crystalline elastomers. *Nat. Rev. Mater.* **7**, 23–38 (2022).
51. V. J. Gokhale, O. A. Shenderova, G. E. McGuire, M. Rais-Zadeh, Infrared absorption properties of carbon nanotube/nanodiamond based thin film coatings. *J. Microelectromech. Syst.* **23**, 191–197 (2014).
52. A. B. Kaul, J. B. Coles, M. Eastwood, R. O. Green, P. R. Bandaru, Ultra-high optical absorption efficiency from the ultraviolet to the infrared using multi-walled carbon nanotube ensembles. *Small* **9**, 1058–1065 (2013).
53. K. Mizuno *et al.*, A black body absorber from vertically aligned single-walled carbon nanotubes. *Proc. Natl. Acad. Sci.* **106**, 6044–6047 (2009).
54. C. J. Chunnilall, J. H. Lehman, E. Theocharous, A. Sanders, Infrared hemispherical reflectance of carbon nanotube mats and arrays in the 5–50 μm wavelength region. *Carbon* **50**, 5348–5350 (2012).
55. N. A. Tomlin, A. E. Curtin, M. White, J. H. Lehman, Decrease in reflectance of vertically-aligned carbon nanotubes after oxygen plasma treatment. *Carbon* **74**, 329–332 (2014).
56. H. Na *et al.*, Hydrogel-based strong and fast actuators by electroosmotic turgor pressure. *Science* **376**, 301–307 (2022).
57. J. Chen, H. Park, K. Park, Synthesis of superporous hydrogels: Hydrogels with fast swelling and superabsorbent properties. *J. Biomed. Mater. Res.* **44**, 53–62 (1999).
58. B. Sun, Z. Wang, Q. He, W. Fan, S. Cai, Porous double network gels with high toughness, high stretchability and fast solvent-absorption. *Soft Matter* **13**, 6852–6857 (2017).
59. X. Liu *et al.*, Ingestible hydrogel device. *Nat. Commun.* **10**, 493 (2019).
60. L.-W. Xia *et al.*, Nano-structured smart hydrogels with rapid response and high elasticity. *Nat. Commun.* **4**, 2226 (2013).
61. Y. Zhou, L. Jin, Hydrolysis-induced large swelling of polyacrylamide hydrogels. *Soft Matter* **16**, 5740–5749 (2020).
62. X. Bao *et al.*, Unusually long polymers crosslinked by domains of physical bonds. *Nat. Commun.* **16**, 4749 (2025).
63. A. Sydney Gladman, E. A. Matsumoto, R. G. Nuzzo, L. Mahadevan, J. A. Lewis, Biomimetic 4D printing. *Nat. Mater.* **15**, 413–418 (2016).
64. F. Oytun, M. U. Kahveci, Y. Yagci, Sugar overcomes oxygen inhibition in photoinitiated free radical polymerization. *J. Polym. Sci. A Polym. Chem.* **51**, 1685–1689 (2013).
65. J. Zheng *et al.*, Mimosa inspired bilayer hydrogel actuator functioning in multi-environments. *J. Mater. Chem. C* **6**, 1320–1327 (2018).
66. B. Han, Y.-L. Zhang, Q.-D. Chen, H.-B. Sun, Carbon-based photothermal actuators. *Adv. Funct. Mater.* **28**, 1802235 (2018).
67. Z. Wang, K. Li, Q. He, S. Cai, A light-powered ultralight tensegrity robot with high deformability and load capacity. *Adv. Mater.* **31**, 1806849 (2019).